Atmos. Chem. Phys. Discuss., 14, 9155–9201, 2014
www.atmos-chem-phys-discuss.net/14/9155/2014/
doi:10.5194/acpd-14-9155-2014

Atmospheric Chemistry and Physics Discussions

Diagnosing the average spatio-temporal impact of convective systems – Part 2: A model inter-comparison using satellite data

M. S. Johnston[1,2], S. Eliasson[2,3], P. Eriksson[1], R. M. Forbes[4], A. Gettelman[5], P. Räisänen[6], and M. D. Zelinka[7]

[1]Department of Earth and Space Sciences, Chalmers University of Technology, Gothenburg, Sweden
[2]Swedish Meteorological and Hydrological Institute, Norrköping Sweden
[3]Department of Computer Science, Electrical and Space Engineering, Division of Space Technology, Luleå University of Technology, Kiruna, Sweden
[4]European Centre for Medium-Range Weather Forecasts, England
[5]National Center for Atmospheric Research, Boulder, Colorado, USA
[6]Finnish Meteorological Institute, Helsinki, Finland
[7]Lawrence Livermore National Laboratory, Livermore, California, USA

Received: 12 March 2014 – Accepted: 24 March 2014 – Published: 4 April 2014

Correspondence to: M. S. Johnston (marston@chalmers.se)

Published by Copernicus Publications on behalf of the European Geosciences Union.

ACPD
14, 9155–9201, 2014

Abstract

The representation of the effect of tropical deep convective (DC) systems on upper-tropospheric moist processes and outgoing longwave radiation (OLR) is evaluated in the climate models EC-Earth, ECHAM6, and CAM5 using satellite observations. A composite technique is applied to thousands of deep convective systems that are identified using local rain rate (RR) maxima in order to focus on the temporal evolution of the deep convective processes in the model and observations.

The models tend to over-produce rain rates less than about $3\,\mathrm{mm\,h^{-1}}$ and under-predict the occurrence of more intense rain. While the diurnal distribution of oceanic rain rate maxima in the models is similar to the observations, the land-based maxima are out of phase. Over land, the diurnal cycle of rain is too intense, with DC events occurring at the same position on subsequent days, while the observations vary more in timing and geographical location.

Despite having a larger climatological mean upper tropospheric relative humidity, models closely capture the observed moistening of the upper troposphere following the peak rain rate in the deep convective systems. A comparison of the evolution of vertical profiles of ice water content and cloud fraction shows significant differences between models and with the observations. Simulated cloud fractions near the tropopause are also larger than observed, but the corresponding ice water contents are smaller compared to the observations. EC-Earth's CF at pressure levels $> 300\,\mathrm{hPa}$ are generally less than the obervations while the other models tend to have larger CF for similar altitudes. The models' performance for ocean-based systems seems to capture the evolution of DC systems fairly well, but the land-based systems show significant discrepancies. In particular, the models have a significantly stronger diurnal cycle at the same geo-spatial position. Finally, OLR anomalies associated with deep convection are in reasonable agreement with the observations. This study shows that such agreement with observations can be achieved in different ways in the three models due to different representations of deep convection processes and compensating errors.

ACPD
14, 9155–9201, 2014

1 Introduction

Simulating moist convection has long been identified as critical if general circulation models (GCMs) are to reasonably represent key features of the tropical climate (Manabe and Strickler, 1964; Manabe and Wetherald, 1967). Cumulus convection occupies a wide range of length and time scales and interacts with many atmospheric processes. Individual clouds are smaller than contemporary GCMs' grid resolution and often grow into large organised clusters covering an area of $\sim 10^3$ km^2. For a general review of tropical convection see Moncrieff et al. (2012). The effects of deep convection are highly parameterized in climate GCMs, but numerical approximation of cumulus convection is a difficult problem (Emanuel, 1991; Arakawa, 2004; Gerard and Geleyn, 2005). Despite continuous improvements in convection parameterization formulations and numerical advances, the representation of convection remains a major contributor to model uncertainty in climate simulations (Randall et al., 2003; Tost et al., 2006; Bechtold et al., 2008).

Previous studies of convective parameterization in GCMs have examined the overall effect of deep convection on simulated atmospheric states and surface precipitation, but there has been less detailed evaluation of the evolution of the convective processes in the model, i.e. from initiation of convection to relaxation back to a mean atmospheric state. Tost et al. (2006) examined four different parameterizations schemes and found large differences in the participating models' precipitation patterns, even though the humidity profiles were close to the observations. Gerard and Geleyn (2005) gave a more detailed examination of the implementation of convective schemes in numerical weather prediction and climate models. Other studies have evaluated GCMs by looking at cloud feedback processes and precipitation connected with convective activity (e.g. Gehlot and Quaas, 2012; Nam et al., 2012). The diurnal cycle of cumulus convection determines the timing of the variations in the upper-tropospheric water, which greatly affects the radiative balance and the surface precipitation in the region (Nesbitt and Zipser, 2003; Allan, 2011). This cycle of tropical convection has long been

ACPD
14, 9155–9201, 2014

a problem for GCMs. Del Genio and Wu (2010) found that GCMs tend to transition too quickly from shallow to deep convection, thereby causing the peak in simulated rain fall to occur hours before observations.

The abundance of passive and active satellite observations in recent years allows a more detailed look at the temporal evolution of the tropical deep convective systems in climate models. Johnston et al. (2013) adapted the compositing method of Zelinka and Hartmann (2009) to diagnose and evaluate the spatio-temporal evolution of ocean-based DC systems, both observed and in GCM, EC-Earth. The composite technique is able to reveal the evolution of the model-simulated DC systems at a high spatio-temporal resolution and thereby evaluate the model's ability to capture the response of upper-tropospheric moist processes to DC systems.

This current study presents a continuation of Johnston et al. (2013), providing a novel application of the composite method with focus on an inter-comparison of the spatio-temporal evolution of DC systems in three GCMs: CAM5, ECHAM6 and EC-Earth version 3. These models all have different parameterizations of convection and moist processes, which greatly influences their representation, evolution, and impacts of deep convective systems. This study also looks at the evolution of DC systems over both ocean and land regions. Similar to Johnston et al. (2013), the ultimate goal is to contribute to further development and improvement of GCMs.

Section 2 provides a brief description of the observational data sources used in the evaluation as well as details of the three models in the comparison. Section 3 describes the compositing technique that is the basis of this study. For a more in depth discussion of the observations and compositing methodology, the reader is referred to Part I of this study in Johnston et al. (2013). Section 4 describes the results of the evaluation and Sect. 5 provides a summary and conclusion.

ACPD
14, 9155–9201, 2014

2 Data

2.1 Review of observations

Data for two full years (2007 and 2008) from primarily polar orbiting satellites are used in this study. Surface hourly rain rates (RR) are taken from the Tropical Rainfall Measurement Mission (TRMM) Multi-satellite Precipitation Analysis (TMPA) 3B42 version 6/6A dataset. The TMPA dataset is constructed using precipitation retrievals from a combination of geostationary and equatorial-orbiting satellites that are scaled using surface rain gauge data (Huffman et al., 2007). Upper-tropospheric humidity (UTH) is provided by the Advanced Microwave Sounding Unit B (AMSU-B) and Microwave Humidity Sounder (MHS) onboard several satellites operated by the National Oceanic and Atmospheric Administration (NOAA) and the European Organisation for Exploration of Meteorological Satellites (EUMETSAT). This dataset is described in Buehler and John (2005). Cloud fraction (CF) and ice water content (IWC) are provided by the CloudSat and Cloud-Aerosol Lidar and Infrared Pathfinder Satellite Observation (CALIPSO) Ice Cloud Property Product (2C-ICE) (Deng et al., 2012). Finally, outgoing longwave radiation (OLR) observations are obtained from the Cloud and Earth Radiant Energy System (CERES) sensors onboard the Aqua and Terra satellites. The data are taken from the Single Satellite Footprint (SSF) cloud edition 3A. Details of the observations datasets used in the study are given in Johnston et al. (2013), and an overview is given in Table 1.

2.2 Description of models

High frequency and high spatial resolution model data are required for this study. The model configurations used for these runs are those stipulated by the Atmospheric Model Inter-comparison Project (AMIP), where the atmospheric GCMs are run using prescribed time series of sea surface temperature and sea ice. Three GCMs participated in this study: EC-Earth version 3 (http://ecearth.knmi.nl), National

ACPD
14, 9155–9201, 2014

Center for Atmospheric Research Community Atmospheric Model version 5 (CAM5), and ECHAM6. Some basic specifications about each model are listed in Table 2. ECHAM6 is the sixth generation of the Max Planck Institute for Meteorology GCM. An overview of this model is given in Stevens et al. (2013) and more technical details can be found online (http://www.mpimet.mpg.de/fileadmin/publikationen/Reports/WEB_BzE_135.pdf). For the CAM5, technical details are given in Neale et al. (2012). EC-Earth's atmospheric component is taken from the European Centre for Medium-Range Forecast (ECMWF) Integrated Forecast System (IFS) Cycle 36r4 (http://www.ecmwf.int/research/ifsdocs).

Similar to the observations, model results for the years 2007 and 2008 are included in the analysis. For CAM5 and ECHAM6, output variables are stored as 3 hourly averages, but EC-Earth's variables include both accumulated and instantaneous fields. The accumulated variables are converted to mean values by dividing by 3 h. The instantaneous variables are interpolated to the centre of the time steps in order to match the accumulated variables.

The reader needs to bear in mind that model output can be defined very differently from the corresponding observations. The observed CF and IWC, derived from radar reflectivity and lidar backscatter, are sensitive to a range of ice particle sizes associated with cloud ice and precipitating snow for all parts of the deep convective systems (including stratiform anvil and convective core). In contrast, the models have distinct representations of different parts of the deep convective systems, which differ between models and are not all generally available from the standard model simulations. All three models have separate categories for stratiform cloud ice, stratiform precipitating snow, and convective precipitating snow. However, only the stratiform cloud ice was available as a standard product from all of the three models. As this has the dominant contribution to IWC in the UT, it is valid to compare with the observations in this study. However, lower in the atmosphere, the precipitating snow IWC becomes more significant and care must be taken in the conclusions drawn from the comparison. Cloud fraction is represented differently in the models, as a prognostic variable in EC-Earth

ACPD
14, 9155–9201, 2014

and diagnostically in ECHAM6 and CAM5, but all tend to be associated with higher relative humidity. The "cloudy" fraction associated with stratiform and convective precipitating snow, which is included in the observed CF, is not included in the model definition of CF. Again this has little impact in the upper troposphere which is dominated by the ice cloud and is the focus of this study, but it does have more of an impact at lower altitudes where the precipitating snow becomes more important.

The number of vertical levels differs between the models (see Table 2), and, when compositing the UTH, IWC, and layered CF, each these output are interpolated to constant pressure levels ranging from 500 to 100 hPa at 50 hPa intervals. Also, the UTH is defined as the mean relative humidity with respect to ice between 500 and 200 hPa.

3 Method

3.1 Composite

The methodology used to compile the results in the form presented is described in detail in Johnston et al. (2013). We have largely continued with this method, with the exception that the data is instead interpolated to a common 1° spatial resolution. Selection of the systems is based on local RR maxima taken from the top 9 percentile of the total RRs (> 0) between ±30° latitude. For TMPA, EC-Earth, ECHAM6, and CAM5, the thresholds for these 9 percentile RRs are approximately 1.5, 0.5, 0.3, and 0.5 mm h^{-1}, respectively. The difference in RR threshold values is due largely to the disparity in RRs between the different datasets (See Sect. 4.1.1). Choosing a percentile rather than an absolute threshold ensures that only the strongest RRs for each dataset are compared. Each DC system's RR forms the centre point for a ±10° latitude and longitude domain. This spatial domain then forms the centre of a time series that extends ±18 h on either side of the time of DC system, the so-called peak RR. Together, these windows form a composite series that captures the evolution of the DC system in each respective dataset. Although individual satellite overpasses cannot provide

ACPD
14, 9155–9201, 2014

complete spatio-temporal coverage of any individual DC system, statistical coverage can be achieved by averaging over many DC systems. Coverage is not a problem for the models as their output is continuous in space and time.

3.2 Regions

The study looks at the statistical effect of DC systems on upper troposphere (UT) moist processes over several regions across the tropics. A separation between land- and ocean-based systems is made, as these differ in certain characteristics, such as their diurnal cycle. The regions depicted in Fig. 1 are selected such that a strict separation between DC systems in the different regions is maintained. The results are analysed within each region, but since there are no major differences between the different regions of similar surface types and for succinctness, all systems over ocean and land regions are merged by taking the mean, weighted by the number of DC systems per region.

4 Results

4.1 Precipitation

The use of surface precipitation as a proxy for identifying DC systems at peak convection necessitates a brief investigation of this aspect of the models. We focus on the normalised probability density function (PDF) of RRs and the diurnal cycle (i.e. the relative occurrence of DC systems per local solar time (LST)).

4.1.1 Rain rate statistics

Table 3 shows the area-weighted mean RR over each region given in Fig. 1 and the combined ocean and land areas. The models tend to produce fairly similar RRs to the observations and to each other over the areas examined. However, the mean

ACPD
14, 9155–9201, 2014

precipitation is systematically overestimated in the models compared to the TMPA observations. Over ocean areas the precipitation can be up to ≈ 30 % higher, while over land areas, the models are closer to the observations.

The probability distribution of RRs for ocean and land regions is shown in Fig. 2. Over both ocean and land, the probability of modelled RRs is larger than observed for RRs $\lesssim 3\,\mathrm{mm\,h^{-1}}$ and smaller than observed for larger RRs. This tendency of excessive light precipitation has been noted previously (e.g. Stephens et al., 2010; Tost et al., 2006). Silmulated RRs above $10\,\mathrm{mm\,h^{-1}}$ are more common than over land, whereas this does not occur in the observations.

4.1.2 Diurnal distribution of DC systems

Figure 3 illustrates the diurnal cycle of the DC systems analysed in this study. The figure shows the relative occurrence of the DC systems as a function of local solar time (LST).

For ocean-based systems, the relative occurrence of TMPA DC systems exhibits a peak from late evening to early morning and a maximum centred around 05:00 LST. A relatively high frequency of DC system occurrence persists into the afternoon.

Over land regions convection begins in the afternoon and culminates in the late evening before tapering off around midnight. For ocean-based systems, there is broad spread in the diurnal distribution of RRs above $10.0\,\mathrm{mm\,h^{-1}}$, but with a minimum occurrence in the afternoon to early evening. Another notable feature of the TMPA observations is the higher frequency of intense land-based DC systems around midnight. Similar findings were reported by Hendon and Woodberry (1993) and Eriksson et al. (2010) who found significant diurnal amplitude of deep convection over land but a weaker cycle over ocean.

The models' ocean-based DC systems show a penchant for deep convection after midnight with a slight drop in the frequency of occurrence in the afternoon to early evening. This is in very good agreement with the observations. While the relative

ACPD
14, 9155–9201, 2014

occurrence of DC systems in ECHAM6 and EC-Earth is of the same order as the observations, CAM5 tends to show a somewhat higher frequency after midnight.

Over land, there is a larger disagreement with the observations. All the models place the bulk of the convective activity roughly between 10:00 and 17:00 LST, which is earlier than the observations. This tendency for land-based convection to occur too early in the day when the solar heating is greatest is a well-known bias in models (e.g. Del Genio and Wu, 2010). The largest modelled RRs appears over the ocean, which is contrary to observations.

4.2 Composites

This section discusses the composites of the RR, UTH, CF, IWC, and OLR. Subsequent sections are dedicated to each variable and discuss ocean- and land-based DC systems, respectively. The reader is reminded that the composites are weighted averages of the land- and ocean-based regions, as well as averages of thousands of DC systems. In addition the term peak convection refers to the 0 h of the composite, and in places where the spatial mean of the composite is averaged temporally, it is simply referred to as the spatio-temporal mean.

4.2.1 Rain rate

Figure 4 depicts the RR composite for ocean- and land-based systems for both observations and models.

For ocean-based systems, the observations show an east-west band of precipitation throughout the time period. Indications of elevated RRs are already present at −12 h, where an area of larger RRs appears in the eastern part of the domain, steadily strengthens, and culminates at peak convection. The elevated region of RRs moves from the eastern to the western portion of the domain as time progresses. This movement of the RR maximum indicates the predominance of westward propagating DC systems in our samples.

ACPD
14, 9155–9201, 2014

The models represent the evolution of the ocean-based DC systems in a very similar manner to the observations. EC-Earth shows the shortest period of elevated RRs, which indicates a shorter convective precipitation process. ECHAM6 and CAM5 are closer to the TMPA dataset, although ECHAM6's region of elevated RR extends over a broader area than that of CAM5 and the observations.

For land-based observed DC systems, from about −18 to −9 h, there is a distinct minimum near the domain centre. As time progresses, a RR maximum, originally located to the east of the domain centre, strengthens and moves towards the domain centre. The strengthening of RRs before peak convection and their decay after appear to have very similar duration. Towards the end of the composite time period, another minimum appears at the spatial centre, similar to the beginning of time period.

Compared to their ocean-based counterparts, the models' land-based DC systems are markedly different in the composite. Notably, the growth and decay of the intense RR region over land occurs over a shorter timescale in the models. This behaviour is apparent especially for EC-Earth and ECHAM6. The spatial signature of the DC systems in ECHAM6 is significantly broader than in the other models and in the observations. The ECHAM6 and EC-Earth also capture the observed minimum in RR at the centre of the domain before and after the main DC event. In contrast, CAM5 has a maximum RR at the centre of the domain that strengthens and weakens in place over the course of the composite, with negligible westward propagation apparent.

In general, simulated RRs are comparable in magnitude to the observations at the core of the DC system, but are weaker than observed away from the center of the domain.

4.2.2 Upper-tropospheric humidity

Figure 5 shows the composite UTH for ocean- and land-based DC systems for the observations and models.

The AMSU observations over ocean areas show a broad band of elevated humidity across most of the domain and throughout the period. However, a very focused region

ACPD
14, 9155–9201, 2014

of humidity exceeding 60 % is apparent at −6 h. This feature increases in spatial coverage and magnitude until about 6 h when a maximum is reached. Afterwards, there is a notable reduction in moisture at the domain centre that continues beyond 18 h. The latitudinal distribution pattern varies from region to region, but the resulting composite indicates that drier areas are generally found to the south of the DC systems.

The models' representations of the effect of ocean-based DC systems on the UTH seem to capture the development and dissipation of the systems. However, the models, especially CAM5, tend to show a moister UT. The spatio-temporal mean UTHs are ∼ 44 % for EC-Earth, ∼ 47 % for ECHAM6, and ∼ 50 % for CAM5, as compared with ∼ 44 % in the AMSU data. However, the maximum UTH across the domain for all models can increase to ∼ 80 %, which is about 10 to 20 percentage points higher than the observations. EC-Earth exhibits a much moister upper troposphere following convection than preceding it, which is rather similar to observations. In contrast, in ECHAM6 and CAM5, UTH remains high throughout the composite and does not exhibit any distinct temporal asymmetry.

The observed UTH pattern is quite different over land. While the oceanic systems are more zonally elongated, the land-based systems are more axi-symmetric. The spatio-temporal mean UTH for these systems is ∼ 52 %, but moisture from DC systems can locally elevate the UTH to over 72 %. There is a clear reduction in UTH from −18 to −6 h followed by rapid increase at the domain centre from time bins −3 to 6 h. This reduction in moisture early in the composite could be explained by the dissipation of earlier convection.

For the land-based systems the models' spatio-temporal mean UTHs are ∼ 51 % for EC-Earth, ∼ 57 % for ECHAM6, and ∼ 61 % for CAM5. These values not only show a significant increase compared with ocean areas but such larger values are also found throughout most of the domain, which is in agreement with the observations.

However, ECHAM6 and CAM5 show significantly higher levels of humidity than the observations over the entire composite domain, with EC-Earth being closest to the AMSU results. While the corresponding observations show a region of slightly elevated

ACPD
14, 9155–9201, 2014

humidity early on the composite sequence, the models indicate much higher UTH values at this juncture.

4.2.3 Cloud fraction

Figure 6 shows the composite average CF at 200 hPa for the 2C-ICE observations and the models. CF is defined using the 2C-ICE dataset where IWC is > 0; thus areas of observed precipitation will also be counted as CF. This must be taken into consideration when interpreting the results.

For the observed ocean-based systems, the mean CF of the domain is on the order of 22 %. There is an increased CF at the domain centre from about −9 to 9 h. Also, close to the domain centre, the spatial mean CF can exceed 70 %.

The models' ocean-based systems show mean CFs across the domain that are slightly larger than observed, ∼ 28 % for EC-Earth, ∼ 29 % for ECHAM6, and ∼ 31 % for CAM5. Generally, CAM5 shows the largest CF across the domain and throughout the composite time period. Elevated levels of CF at the domain centre can be seen in EC-Earth from about 0 to 12 h, but in ECHAM6 and CAM5 this pattern is not as easily discerned. Thus, as was the case with UTH, only EC-Earth is able to capture the observed temporal asymmetry with respect to hour 0. The observed land-based systems show a mean CF that is higher than for ocean-based systems by about 8 percentage points, and locally the CF can reach up to 80 %. Observed CF remains anomalously large for about 9 h following convection, and is largest at 3 h. About 3 h after peak convection there is a marked increase in the CF that lasts about 9 h. Both the models and observations place the spatial maximum CF (70–80 %) between 3 and 6 h, but as time progresses the high CF at the domain centre spreads out across the domain until about 15–18 h.

Consistent with the results of the simulated UTH over land, more cloudiness is generated for simulated land-based DC systems. The spatio-temporal mean CFs in CAM5, EC-Earth, and ECHAM6 are higher by about 13 and 6 percentage points respectively. ECHAM6, however, shows only an increase of less than 1 percentage point. Again,

ACPD
14, 9155–9201, 2014

the models, between themselves, show similar CF maxima attained within the domain of ∼ 78 %. Similar to the UTH, the spatial patterns of the simulated CFs are broader over land and display a somewhat axial symmetry with respect to the domain centre. For these systems, the models show a similar pattern of decreased CF as time approaches peak convection, before increasing again towards 18 h. However, ECHAM6 shows a much faster reduction in CF by 15 h than the other two models.

4.2.4 CF time–altitude anomaly

Figure 7 illustrates the CF anomalies as a function of both pressure and time. In this figure, the time bins span ±48 h, and the data are averaged over ±3° latitude, ±10° longitude from the domain centre point in order to better focus on the DC systems' core region. The anomaly is derived by subtracting the background state, which is taken as the average of the time bins −48 to −39 h. For this figure, the data are averaged over ±3° latitude, ±10° longitude from the centre point. Because the observations tend to be noisy, the spatio-temporal pattern of the anomaly in the figure emerges only after applying a 12 h running average. Such smoothing is not applied to the models as they are not significantly affected.

Over ocean regions, the observed CF anomaly associated with DC is vertically coherent, with CF increasing by about 10 percentage points between ±5 h at all levels. A maximum CF anomaly of about 12 percentage points covers a region between 250 and 150 hPa between peak convection and 10 h. A secondary positive CF anomaly, which is not fully separate from the one at peak convection, appears at ∼ 20 h. In addition, a series of positive CF anomalies is seen in the uppermost troposphere (∼ 100–150 hPa) centred at ∼ −27, −3, 21 and 45 h. This pattern is associated with a diurnal cycle and occurs a few hours after the time of peak RR. A contributor to the anomaly's vertically uniform structure is the larger precipitating hydrometeors being included in the definition of the cloud fraction.

The modelled CF anomalies for ocean-based systems vary greatly among themselves and look quite different from the observations. The greatest concordance

ACPD
14, 9155–9201, 2014

between the models and observations occurs between 300 and 100 hPa. Elsewhere, there are major differences. For EC-Earth, the anomaly at pressure levels > 300 hPa is significantly lower than the observations. This disparity can partly be explained by the lack of a precipitating component in the model's CF. ECHAM6 and CAM5 anomalies show similar magnitudes as the observations, but are sustained over a much longer duration at pressure levels > 300 hPa. The CAM5 anomalies at peak convection and 24 h seem to merge, suggesting a repetition of DC systems that causes the CF anomaly to persist for twice as long as in the observations. Evidence of the models' diurnal cycle of convection can be seen in the ocean-based systems around −24, 24, and 48 h. The duration of the EC-Earth and ECHAM6 CF anomalies is comparable to the observations, but in contrast, CAM5 shows a longer duration. The simulated positive CF anomalies of all the models tend to last longer than in the observations, persisting at least 48 h after peak convection.

For land regions, the observed CF anomaly is weaker and of shorter duration than for ocean-based systems. The largest CF anomaly is located near 200 hPa between 0 and 12 h, and it persists for a much shorter time, ≈ 12 h vs. ∼ 20 h for ocean-based systems. A diurnal cycle of negative CF anomalies can be seen around −33, −9, 15 and 39 h. A secondary, and much weaker, CF maximum is seen about 24 h after peak convection, while at −24 h, the cloud fraction anomaly is slightly negative.

The models' land-based DC systems show much greater disparity with the observations. Most notably, a stronger diurnal cycle of CF anomalies is present in the models than in the observations at the same location. Within ±48 h, all models show 4 distinct anomalies of similar magnitudes, whereas the observations only indicate one clear case, centred at hour 0. The observed positive land-based CF anomalies begin at 0 h, but the models seem to start later relative to the time of maximum RR. There is also a distinct tilt in the model anomalies, which appear first at high levels, then propagate downward. This is less obvious in the observations. While the observations do indicate some activity around −21 and 27 h, these CF anomalies are significantly smaller than in the models by up to 10 percentage points. This suggests that the models might be

ACPD
14, 9155–9201, 2014

triggering deep convection too often at the same place. Similar to the observations, EC Earth's cloud fraction anomalies are greatest around 250 hPa and decrease with increasing pressure. CAM5 and ECHAM6 do not show this decrease in their anomalies at these higher pressure levels.

4.2.5 Cloud ice water content

Individual GCMs parameterize IWC differently, and this is reflected in the results. See Johnston et al. (2012) for an in-depth look of the treatment of ice in EC-Earth and Waliser et al. (2009) for a general overview of this treatment in a number of models from the Coupled Model Intercomparison Project, 3rd Phase. In particular, it is of note that the IWC available from the models only includes stratiform cloud ice and lacks the snow hydrometeors from the stratiform and convective parameterizations that are present in the observed estimates of IWC. However, most probably, this does not greatly affect the general spatio-temporal distribution of IWC in these upper levels. To demonstrate this, CAM5's large-scale snow was added to the suspended ice (not shown). Although at lower altitudes this added significant IWC, at 200 hPa the increase in IWC is small and the spatio-temporal patterns are the same. While it is possible to perform some separation of precipitating and non-precipitating ice, as suggested by Chen et al. (2011), the models do not all partition these categories of ice along clear and generally well-defined particle sizes. This fact makes it difficult to partition the observations to match a set of models. Nevertheless, the models' standard IWC is enough for a first step comparison where the focus is on the general spatio-temporal patterns.

The mean IWC at 200 hPa for the 2C-ICE observations and the models is shown in Fig. 8. In the observations over the ocean, elevated values of IWC cover a broad portion of the domain in each time bin with somewhat zonally elongated regions of elevated IWC at the domain centre.

Away from the domain centre, IWC values up to $\sim 20\,\mathrm{mg\,m^{-3}}$ are present throughout the composite. Between −9 and 6 h, the IWC increases sharply to $\sim 70\,\mathrm{mg\,m^{-3}}$ near

ACPD
14, 9155–9201, 2014

the domain centre. This region with a sharp, near-radially symmetric gradient relaxes quickly after peak convection.

Over ocean, the models show the typical zonally elongated spatial patterns of IWC similar to the observations. Among the models, EC-Earth reports the highest amount of ice at this level with spatial mean values of ~ 2 to $15\,\mathrm{mg\,m^{-3}}$. CAM5 and ECHAM6 have considerably lower IWC with spatial mean values $\lesssim 3\,\mathrm{mg\,m^{-3}}$. In the models elevated values of IWC at the domain centre appear first around 0 h and last until approximately 9 h.

Over land, the observed IWC in each time bin also shows broad spatial coverage of values $\gtrsim 30\,\mathrm{mg\,m^{-3}}$. However, for these systems, the domain centre is a focal point rather than a part of a zonally elongated region of elevated values, much like the RR patterns. Between hours −6 and 6, enhanced IWC is present at the domain centre with values similar to those seen in the ocean-based composite. The spatio-temporal mean IWC over land regions is $\approx 19\,\mathrm{mg\,m^{-3}}$, which is nearly twice as large as that over ocean regions ($\approx 11\,\mathrm{mg\,m^{-3}}$).

For land-based systems, EC-Earth is again the model with the most ice. The spatio-temporal mean IWC for land-based systems is also greater than that for the ocean-based systems, as in the observations. The IWC displays a radially symmetric spatial pattern which is in good agreement with the observations. In all models, there is evidence of elevated IWC at the domain centre at −18 h, which then decreases as time approaches 0 h, before again rising sharply. This points to a strong diurnal cycle in the IWC, consistent with the CF and other upper-tropospheric quantities.

4.2.6 IWC time–altitude anomaly

In Fig. 9 the temporal effect of DC systems on the vertical distribution of IWC is examined. Similar to the CF, only the observed time–altitude IWC anomalies are smoothed. Large inter-model differences and model-observation differences in the diurnal cycle, the placement of ice both vertically and in time, and the magnitude of the IWC anomalies are evident in Fig. 9.

ACPD
14, 9155–9201, 2014

The observations over oceanic areas show a strong response to the DC systems that extends throughout most of the UT to about 150 hPa. Upper-tropospheric IWC anomalies emerge some time around −12 h with the maximum IWC values occurring at 3 h and between 500 and 250 hPa. Also, between these pressure levels, ocean-based systems show the greatest increase in IWC with a duration of about ∼ 30 h. The IWC anomalies increase with increasing pressure above the 450 hPa level, being ∼ 5 mg m^{-3} between 150 and 200 hPa, and ∼ 20 mg m^{-3} between 400–500 hPa. There is an indication of a diurnal cycle in these anomalies, which is most distinct at pressure levels < 300 hPa. Finally, there is a notable tilt, where IWC anomalies belonging to the same DC system appear earlier in time at lower pressure levels than at higher pressure levels. This tilt is equally pronounced over land and ocean areas. This feature could partly be the result of the rate of ice particle formation, and the sedimentation of stratiform cloud ice. However, further investigation into these aspects is beyond the scope of this study.

Over ocean areas, the spatio-temporal structure of simulated IWC anomalies varies greatly from the observations. The vertical distribution pattern of CAM5's anomalies indicates that the IWC response to DC systems occurs mainly at pressure levels between 350 and 150 hPa. The magnitude of the IWC response in CAM5 is on the order of ∼ 1 mg m^{-3}, which is the lowest of all the models. At pressure levels > 350 hPa, CAM5's IWC anomalies reduce to zero, which is largely due to the exclusion of the snow components of the IWC. ECHAM6's IWC anomaly is limited to pressure levels > 200 hPa and its maximum of ∼ 3 mg m^{-3} occurs around 350 hPa. Near 500 hPa, ECHAM6's anomaly approaches zero, which is also due to the exclusion of snow. The spatio-temporal distribution of the EC-Earth anomaly is closest to the observations, with roughly three distinct plumes that penetrate the UT to pressure levels close to 100 hPa. The largest IWC anomalies for the models are ∼ 1 mg m^{-3} for CAM5, ∼ 2 mg m^{-3} for EC-Earth and ∼ 3 mg m^{-3} for ECHAM6, which are all much smaller than the observed anomalies. Furthermore, although there is a hint of a tilt in the IWC profiles at pressures less than 300 hPa for EC-Earth and CAM5 (i.e. the signal first appearing at the upper levels and

ACPD
14, 9155–9201, 2014

then proceeding downwards), none of the models' ocean-based systems appear to exhibit the tilt in the anomaly for pressures greater than 300 hPa seen in the observations.

The simulated ocean-based anomalies have more diffuse diurnal cycles relative to those over land. CAM5 has virtually no additional anomalies apart from peak convection. ECHAM6 shows additional anomalies at approximately hours ±36 h and ±12 h, which is an indication of its diurnal cycle. The anomalies of EC-Earth occur at ±24 h in addition to peak convection. Unlike EC-Earth and the observations, the IWC anomalies corresponding to peak convection of CAM5 and ECHAM6 are not centred at 0 h, which could indicate that detrained ice remains as anvil cirrus for a longer time.

Observed land-based DC systems penetrate the UT to slightly lower pressure levels than their ocean-based counterparts. The duration of the anomaly is ∼ 20 h. The diurnal cycle is quite dissimilar between these different systems. Over the ocean areas there are two notable peaks in the IWC anomaly at ≈ ±24 h. Out of these, the anomaly after peak convection is stronger than the one prior to it; however, both anomalies are significantly weaker than the main system anomaly centred at 0 h.

Over land, the agreement between the models is better, and all show a strong diurnal cycle of convection. The land-based anomalies show a shorter and more distinct duration than the ocean-based systems. EC-Earth and CAM5 show similar values of $\sim 2\,\mathrm{mg\,m^{-3}}$, but ECHAM6 anomalies show a larger increase at pressures greater than 300 hPa to values of around $\sim 9\,\mathrm{mg\,m^{-3}}$. For these systems, the models show some tilt in the anomalies. Above 300 hPa, the timing of the peak diurnal IWC anomaly, associated with the stratiform anvil cloud, is similar for all models (as also shown for 200 hPa in Fig. 8), with a slight delay behind the observed anomaly of 3 to 6 h. However, below 300 hPa the timings of the IWC anomalies are very different. The main anomalies of CAM5 and ECHAM6 are about 12 h out of phase with the observations relative to peak RR. In contrast, EC-Earth's anomalies are centred on peak convective RR and ±24 h, which is close to the observations. CAM5 also has a hint of increased IWC between 400 and 450 hPa with similar timing. However, the tilt in the model anomalies reaches back farther in time than in the observations. The reason for these differences

ACPD
14, 9155–9201, 2014

requires further investigation but may be related to the different convective detrainment formulations in the models. All models have slightly larger IWC following the main event compared to ±24 h, but the difference is not as marked as in the observations. Including stratiform and convective precipitating snow components from the models would increase the IWC significantly at these lower levels, may change the timing of peak anomaly and would be a fairer comparison with the observed IWC, but unfortunately are not available for all models for this study.

4.2.7 Outgoing longwave radiation

The CERES OLR observations shown in Fig. 10 for both ocean and land DC system types are in fair agreement with the spatial patterns seen in the AMSU UTH observations. The ocean-based systems show a decrease in OLR at the domain centre of the composite at approximately −9 h. The minimum in OLR is not located at 0 h but rather around 3 h, which suggest a maximum coverage by anvil clouds around that time. The spatial coverage of the OLR minimum at 3 h is about 300 km × 400 km, which is in agreement with the dimensions of convective clusters (Houze, 1989, Fig. 2). Relaxation of the OLR back to the mean state occurs between 15 and 18 h.

For ocean-based systems, all models show an emergence and dissipation of area of minimum OLR at the domain centre. For ECHAM6 and EC-Earth, this first appears roughly between time bins −6 and −3 h and lasts until around 9 h. However, CAM5's minimum appears at −15 and lasts beyond 18 h, which is similar to the observations. The models show zonal bands of high OLR both north and south on the domain, but the observations show only a narrow band of higher OLR to the south. This suggests that models are allowing more OLR to escape into space than seen in the observations. This could be caused by the extent of the model DC systems' CF being too zonally narrow, in particular at the northern boundary of the domain. However, since the vertical extent of the simulated clouds is comparable to observations (Fig. 7) and there is a distinct overproduction of CF at 200 hPa (Fig. 6), the most probable explanation for the higher than observed OLR is that the IWC is underestimated (Fig. 8), which makes

ACPD
14, 9155–9201, 2014

the model clouds too transparent. At the domain centre of the DC systems, CAM5's spatial pattern is closest to the observations, as the other models overestimate OLR at the domain centre.

The observed land-based systems, similar to the composite results of the other variables, are markedly different from those over oceans. There is a distinct increase in the OLR from time bins −18 to −6 h, which suggests a relaxation from earlier convection. Indications of the DC systems can be seen sometime between −6 and −3 h, which lasts until about 15 h. For both type of DC systems, the OLR can locally fall below 180 $W m^{-2}$, however, the spatial coverage of the OLR minimum is larger than for ocean-based systems, roughly 400 km × 400 km.

Over land, all the models agree quite well with CERES in showing a decrease in OLR starting between −3 and 0 h, but the spatial extent of the decrease in OLR is consistently smaller in the models. Throughout the temporal extent of the composite there is a notable absence of higher OLR at the edge of the domain. This suggests that the clouds generated by land-based systems have a far greater spatial coverage than ocean-based systems, which agrees well with the observations. EC-Earth and ECHAM both show similar diurnal effects in time bins −18 to around −3 h, where the OLR is increasing, quite likely in response to dissipating clouds from earlier convection. The timing of minimum OLR is distinct in ECHAM6 and EC-Earth that place it around 3 h. In CAM5 the minimum is not very clear and occurs sometime between 3 and 9 h. The overall effect of the DC systems on OLR lasts longer in CAM5 than in the other two models, consistent with the slower decay of IWC (Fig. 8). In both ECHAM6 and EC-Earth, cloud dissipation after peak convection takes about 18 h, which is faster than in the observations.

Both over ocean and land, the spatial coverage of the area showing decrease in OLR at the centre of the models' domain is consistently smaller than in the observations.

ACPD
14, 9155–9201, 2014

4.2.8 Zonal propagation of convection

Figure 11 shows Hovmöller diagrams of RR as a function of longitude and time for a randomly-chosen seven day period in the observations and models, and provides an indication of the motion of convective activity. Following Blackburn et al. (2013, Fig. 16), only activity between ±5° latitude is examined. Similar to Johnston et al. (2013, Fig. 7), Hovmöllers, but averaged over all DC systems included in the composites, separately for ocean-based and land-based convection, are shown in Fig. 12.

The observed propagation during the 7 days examined shows convection moving zonally in both directions. The predominant motion around 60 and 120° E appears to be eastward, but around 180 and 60° W the motion is opposite. Furthermore, at some meridians, both eastward and westward motions occur but at different times. When averaged, the observed DC systems tend to show a westward motion, regardless of surface type. This could be interpreted as fast-moving systems moving west embedded within slower moving envelopes of convection moving east.

Models also exhibit zonally propagating convection. As in the observations, both westward and eastward propagating equatorial waves are present in the models. These results are in agreement with Blackburn et al. (2013) who examined the motion of equatorial precipitation for a 30 day period for 16 different models and found similar differences between a range of models. When the motion of the mean DC systems is examined (Fig. 12), EC-Earth shows some clear motion of the DC systems over ocean but primarily towards the east. The remaining models show no clear zonal motion of these systems. Over land, none of the models shows zonal motion.

Another interesting feature of Fig. 12 is the occurrence of convection at ±24 h. Over ocean, the observations and the models all tend to place successive convection westward in time. The simulated land-based DC systems in Fig. 12, on the other hand, show a diurnal cycle of convection of nearly similar intensity at the same longitude, which is not seen in the observations.

ACPD
14, 9155–9201, 2014

5 Summary and conclusion

This study highlights the evolution of tropical deep convective systems over ocean and land in three prominent GCMs (EC-Earth, ECHAM6, and CAM5) and compares them with a range of satellite-based observations. A composite technique is employed to compile model and observational data around thousands of deep convective systems that are identified using local rain rate maxima. The ability of this technique to capture the evolution of deep convection in a GCM is demonstrated in Johnston et al. (2013). The effects of deep convection are investigated and compared for several upper tropospheric variables related to moist processes (relative humidity, cloud fraction, and ice water content) and outgoing longwave radiation.

The models capture the evolution of deep convection in a largely similar manner to what is observed, but there are significant aspects of simulated DC systems that diverge from the observations. When considering the total RR across the tropics, the models show an over-production of light precipitation ($\lesssim 3\,\mathrm{mm\,h^{-1}}$) and an underestimation of the occurrence of higher RR intensities compared to the TMPA RR observations. The diurnal distribution of the DC system RRs in the models is similar to the observations for ocean-based systems, however, land-based systems peak several hours too early. Both of these are common problems in GCMs that have been previously identified but are important to show as this study relies on the RR as defining the deep convective events. The models' UTHs agree qualitatively with the observations, however, all the models tend to be have higher relative humidities, with CAM5 having the highest UTH. Nevertheless, the models show a similar effect of DC systems on the cloud fractions at 200 hPa, similar to the observed CF derived from the 2C-ICE dataset. CAM5, however, consistently reports higher CFs across the domain for both land and ocean-based systems.

The observed cloud fraction includes the presence of all hydrometeors, whereas the representation of cloud fraction in the models varies. For EC-Earth, CF is a prognostic variable with sources from convective detrainment and nucleation of cloud ice.

ACPD
14, 9155–9201, 2014

The hydrometeor fraction associated with the precipitating snow category is not included, and hence the CF is significantly lower than the observations for pressure levels > 300 hPa. In contrast, CF is a diagnostic variable in ECHAM6 and CAM5 and although similarly there is no fraction associated with precipitating snow, the CF is significantly higher at these lower altitudes for these two models. Over ocean areas, the modelled CF anomalies reach their maximum at levels close to 200 hPa. While this is also true for EC-Earth over land, the CAM5 and ECHAM6 anomaly maxima are spread out throughout the upper troposphere almost simultaneously. While the models' performance for ocean-based systems seems to capture the evolution of DC systems fairly well, the land-based systems show significant discrepancies. In particular, the models have a significantly stronger diurnal cycle at the same geo-spatial position.

The observed spatio-temporal mean IWCs at 200 hPa are $\sim 11\,\mathrm{mg\,m^{-3}}$ over ocean and $\sim 19\,\mathrm{mg\,m^{-3}}$ over land. DC systems can raise these IWCs in proximity to the convective domain centre to $\sim 70\,\mathrm{mg\,m^{-3}}$, which decreases rapidly after peak convection. Although the spatio-temporal mean IWCs differ, the magnitudes of the anomalies are about the same for land- and ocean-based systems. However, there are significant uncertainties in observed IWC (Austin et al., 2009). These uncertainties are a hinder to properly constraining the simulated IWC values, which contributes to the variation in the model results. Information about the different phases in upper-tropospheric water is difficult to retrieve from satellites, and, therefore, the 2C-ICE product is strongly sensitive to assumptions about ice fraction and temperature. This points to the need for pseudo-satellite simulators in future comparisons of observed and simulated IWC.

The models are able to capture the overall statistical spatial patterns of IWC over both land and ocean at 200 hPa. EC-Earth reports the greatest amount of ice at this level with spatial mean values of ~ 2 to $15\,\mathrm{mg\,m^{-3}}$ for both system types. CAM5 and ECHAM6 have considerably lower spatial mean values below $< 3\,\mathrm{mg\,m^{-3}}$. Similar IWC magnitudes for earlier versions of these models were found by Eriksson et al. (2010) using retrievals from CloudSat and Odin. The maximum IWC at 200 hPa, for each model,

ACPD
14, 9155–9201, 2014

lasts about 9 h and is consistently lower in magnitude than observed, even when adding in the stratiform snow component to the IWC in CAM5.

The observed time–altitude IWC anomalies over both surface types reach 100 hPa. Anomalies for maritime systems emerge roughly about 10 h prior to maximum convection with peak values between ≈ 500 and 250 hPa. Ocean-based systems show a greater increase in IWC anomaly and with a longer duration than for land-based ones, ∼ 30 vs. ∼ 20 h respectively. Between 200 and 100 hPa, the anomaly can reach $\sim 5\,\mathrm{mg\,m^{-3}}$, but at higher pressure levels this anomaly can be up to four times larger.

The modelled time–altitude IWC anomalies over land have a strong diurnal cycle for deep convection. Over ocean, this diurnal cycle is less distinct. Such a strong diurnal signal in the models suggests that they have more of a tendency for convection to trigger at the same location from day to day than in the observations, or possibly an inability to capture the variability in convective strength from day to day. The timing of the IWC at pressures < 300 hPa is similar, but the behaviour for pressures > 300 hPa is very different in the different models. EC-Earth's IWC anomalies are centred around peak convection, which is close to the observation peak at these levels. CAM5 shows a hint of this signal around 450 hPa but the main IWC anomalies of CAM5 and ECHAM6 are both centred 12 h out of phase with the observations. The latter feature may be related to the fact that the majority of precipitation is diagnostic from the convective precipitating snow, which will be maximum at peak RR, but was not available for the comparison. However, the comparison does highlight significant differences in the representation of cloud ice associated with DC systems and could be the subject of further investigation beyond the scope of this study.

The spatial coverage of observed DC systems' clouds over ocean is typically 300 km × 400 km, which is in agreement with Houze (1989, Fig. 2). The land-based systems tend to cover an even larger area. For both types of DC system, the OLR can locally fall below $180\,\mathrm{W\,m^{-2}}$. The models agree with the observations with regards to the minimum OLR reached within the DC systems. However, for ocean-based systems, the models are consistently warmer than the observations outside the domain

ACPD
14, 9155–9201, 2014

centre. This is due to the smaller spatial effect of the models' DC systems. Over land, all the models agree quite well with CERES in showing a similar timing in the OLR minimum, slightly after the peak RRs, but the spatial extent of OLR decrease is consistently smaller in the models.

Propagation of tropical convection in connection with zonally moving waves, as seen in the observations, is captured by the models. However, when focusing on DC systems the motion is either absent of contrary to what is observed. For example, any such motion is absent from land-based systems, while only EC-Earth and ECHAM6 show some propagation for ocean-based systems, with EC-Earth's systems apparent movement mostly opposite to that seen in the observations.

This study has evaluated the representation of the effects of tropical deep convective systems on the upper-troposphere for three global climate models using a novel compositing technique to focus on the temporal evolution compared to satellite observations. The evaluation highlights a good degree of agreement of the spatio-temporal patterns of UTH, cloud fraction, ice water content and OLR in the UT around 200 hPa between all the models and the observations. However, there are significant differences in the magnitude and exact timing of the anomalies relative to the time of peak surface rain rate. Similar OLR in the models is achieved with different cloud fractions and ice water contents and highlights the potential for compensating errors in the models leading to reasonable radiative fluxes. A key motivation for this study is to identify systematic errors in multiple cloud related quantities to inform model development, so that the correct radiative fluxes can be achieved in models for the right reasons. The study also highlights the difficulties of comparing cloud fraction and ice water contents due to the different representation and definitions between models and observations. Additional model output including all components of the IWC should be available as standard from global climate model simulations in the future in order to perform a fair comparison with observations, either through the use of model forward operators or geophysical retrievals. The detailed representation of deep convection through parameterization in GCMs remains a challenge, particularly for the temporal evolution and

ACPD
14, 9155–9201, 2014

lifecycle of organised convection (Moncrieff et al., 2012) and Tobin et al. (2013) and there is certainly scope for further in depth evaluations to inform parameterization development and improve global climate models.

Acknowledgements. The work of M. D. Z. Zelinka is supported by the Regional and Global Climate Modeling Program of the Office of Science at the US Department of Energy (DOE) and is performed under the auspices of the US DOE by Lawrence Livermore National Laboratory under Contract DE-AC52-07NA27344. The National Center for Atmospheric Research is sponsored by the US National Science Foundation. Patrick Eriksson is supported by the Swedish National Space Board. The TMPA data were provided by the NASA/Goddard Space Flight Center's Mesoscale Atmospheric Processes Laboratory and PPS, which develop and compute the TMPA as a contribution to TRMM. In addition the CERES data were obtained from the NASA Langley Research Center Atmospheric Science Data Center. The authors would also like to acknowledge the NASA CloudSat project that provided the CloudSat-CALIPSO dataset used in this project.

References

Allan, R. P.: Combining satellite data and models to estimate cloud radiative effect at the surface and in the atmosphere, Meteor. Appl., 18, 324–333, doi:10.1002/met.285, 2011. 9158

Arakawa, A.: The Cumulus Parameterization Problem: past, present, and future, J. Climate, 17, 2493–2525, doi:10.1175/1520-0442(2004)017<2493:RATCPP>2.0.CO;2, 2004. 9158

Austin, R. T., Heymsfield, A. J., and Stephens, G. L.: Retrieval of ice cloud microphysical parameters using the CloudSat millimeter-wave radar and temperature, J. Geophys. Res., 114, D00A23, doi:10.1029/2008JD010049, 2009. 9179

Bechtold, P., Chaboureau, J. P., Beljaars, A., Betts, A. K., Köhler, M., Miller, M., and Redelsperger, J. L.: The simulation of the diurnal cycle of convective precipitation over land in a global model, Q. J. Roy. Meteor. Soc., 130, 3119–3137, doi:10.1256/qj.03.103, 2004. 9188

Bechtold, P., Köhler, M., Jung, T., Doblas-Reyes, F., Leutbecher, M., Rodwell, M. J., Vitart, F., and Balsamo, G.: Advances in simulating atmospheric variability with the ECMWF model: from synoptic to decadal time-scales, Q. J. Roy. Meteor. Soc., 134, 1337–1351, doi:10.1002/qj.289, 2008. 9158, 9188

ACPD

14, 9155–9201, 2014

Blackburn, M., Williamson, D. L., Nakajima, K., Ohfuchi, W., Takahashi, Y. O., Hayashi, Y.-Y., Nakamura, H., Ishiwatari, M., McGregor, J. L., Borth, H., Wirth, V., Frank, H., Bechtold, P., Wedi, N. P., Tomita, H., Satoh, M., Zhao, M., Held, I. M., Suarez, M. J., Lee, M.-I., Watanabe, M., Kimoto, M., Liu, Y., Wang, Z., Molod, A., Rajendran, K., Kitoh, A., and Stratton, R.: The Aqua-Planet Experiment (APE): CONTROL SST simulation, J. Meteorol. Soc. Jpn., 91A, 17–55, doi:10.2151/jmsj.2013-A02, 2013. 9177

Buehler, S. A. and John, V. O.: A simple method to relate microwave radiances to upper tropospheric humidity, J. Geophys. Res., 110, D02110, doi:10.1029/2004JD005111, 2005. 9160

Chen, W.-T., Woods, C. P., Li, J.-L. F., Waliser, D. E., Chern, J.-D., Tao, W.-K., Jiang, J. H., and Tompkins, A. M.: Partitioning CloudSat ice water content for comparison with upper-tropospheric ice in Global Atmospheric Models, J. Geophys. Res., D19206, doi:10.1029/2010JD015179, 2011. 9171

Del Genio, A. D. and Wu, J.: The role of entrainment in the diurnal cycle of continental convection, J. Climate, 23, 2722–2738, doi:10.1175/2009JCLI3340.1, 2010. 9159, 9165

Deng, M., Mace, G. G., Wang, Z., and Lawson, R. P.: Evaluation of several A-Train ice cloud retrieval products with in situ measurements collected during the SPARTICUS campaign, J. Appl. Meteorol. Clim., 52, 1014–1030, doi:10.1175/JAMC-D-12-054.1, 2012. 9160

Emanuel, K. A.: A scheme for representing cumulus convection in large-scale models, J. Atmos. Sci., 48, 2313–2329, doi:10.1175/1520-0469(1991)048<2313:ASFRCC>2.0.CO;2, 1991. 9158

Eriksson, P., Rydberg, B., Johnston, M., Murtagh, D. P., Struthers, H., Ferrachat, S., and Lohmann, U.: Diurnal variations of humidity and ice water content in the tropical upper troposphere, Atmos. Chem. Phys., 10, 11519–11533, doi:10.5194/acp-10-11519-2010, 2010. 9164, 9179

Forbes, R. M., Tompkins, A. M., and Untch, A.: A new prognostic bulk microphysics scheme for the IFS, ECMWF Technical Memoranda 649, ECMWF, available at: http://www.ecmwf.int/publications (last access: 4 April 2014), 2011. 9188

Gehlot, S. and Quaas, J.: Convection–climate feedbacks in the ECHAM5 General Circulation Model: evaluation of cirrus cloud life cycles with ISCCP satellite data from a lagrangian trajectory perspective, J. Climate, 25, 5241–5259, doi:10.1175/JCLI-D-11-00345.1, 2012. 9158

Gerard, L. and Geleyn, J.-F.: Evolution of a subgrid deep convection parametrization in a limited-area model with increasing resolution, Q. J. Roy. Meteor. Soc., 131, 2293–2312, doi:10.1256/qj.04.72, 2005. 9158

ACPD
14, 9155–9201, 2014

Gettelman, A., Morrison, H., and Ghan, S. J.: A new two-moment bulk stratiform cloud microphysics scheme in the community atmosphere model, Version 3 (CAM3). Part II: Single-column and global results, J. Climate, 21, 3660–3679, doi:10.1175/2008JCLI2116.1, 2008. 9188

Hendon, H. H. and Woodberry, K.: The diurnal cycle of tropical convection, J. Geophys. Res.-Atmos., 98, 16623–16637, doi:10.1029/93JD00525, 1993. 9164

Houze, R. A.: Observed structure of mesoscale convective systems and implications for large-scale heating, Q. J. Roy. Meteor. Soc., 115, 425–461, doi:10.1002/qj.49711548702, 1989. 9175, 9180

Huffman, G. J., Bolvin, D. T., Nelkin, E. J., Wolff, D. B., Adler, R. F., Gu, G., Hong, Y., Bowman, K. P., and Stocker, E. F.: The TRMM Multisatellite Precipitation Analysis (TMPA): quasi-global, multiyear, combined-sensor precipitation estimates at fine scales, J. Hydrometeorol., 8, 38–55, doi:10.1175/JHM560.1, 2007. 9160

Johnston, M. S., Eriksson, P., Eliasson, S., Jones, C. G., Forbes, R. M., and Murtagh, D. P.: The representation of tropical upper tropospheric water in EC Earth V2, Clim. Dynam., 39, 2713–2731, doi:10.1007/s00382-012-1511-0, 2012. 9171

Johnston, M. S., Eliasson, S., Eriksson, P., Forbes, R. M., Wyser, K., and Zelinka, M. D.: Diagnosing the average spatio-temporal impact of convective systems – Part 1: A methodology for evaluating climate models, Atmos. Chem. Phys., 13, 12043–12058, doi:10.5194/acp-13-12043-2013, 2013. 9159, 9160, 9162, 9177, 9178

Lohmann, U. and Roeckner, E.: Design and performance of a new cloud microphysics scheme developed for the ECHAM general circulation model, Clim. Dynam., 12, 557–572, doi:10.1007/BF00207939, 1996. 9188

Manabe, S. and Strickler, R. F.: Thermal equilibrium of the atmosphere with a convective adjustment, J. Atmos. Sci., 21, 361–385, http://dx.doi.org/10.1175/1520-0469(1964)021<0361:TEOTAW>2.0.CO;2, 1964. 9158

Manabe, S. and Wetherald, R. T.: Thermal equilibrium of the atmosphere with a given distribution of relative humidity, J. Atmos. Sci., 24, 241–259, doi:10.1175/1520-0469(1967)024<0241:TEOTAW>2.0.CO;2, 1967. 9158

Moncrieff, M. W., Waliser, D. E., and Caughey, J.: Progress and direction in tropical convection research: YOTC international science symposium, B. Am. Meteorol. Soc., 93, ES65–ES69, doi:10.1175/BAMS-D-11-00253.1, 2012. 9158, 9182

ACPD
14, 9155–9201, 2014

Morrison, H. and Gettelman, A.: A new two-moment bulk stratiform cloud microphysics scheme in the community atmosphere model, version 3 (CAM3). Part I: Description and numerical tests, J. Climate, 21, 3642–3659, doi:10.1175/2008JCLI2105.1, 2008. 9188

Nam, C., Bony, S., Dufresne, J.-L., and Chepfer, H.: The "too few, too bright" tropical low-cloud problem in CMIP5 models, Geophys. Res. Lett., 39, L21801, doi:10.1029/2012GL053421, 2012. 9158

Neale, R. B., Chen, C.-C., Gettelman, A., Lauritzen, P. H., Park, S., Williamson, D. L., Conley, A. J., Garcia, R., Kinnison, D., Lamarque, J.-F., Marsh, D., Mills, M., Smith, A. K., Tilmes, S., Vitt, F., Morrison, H., Cameron-Smith, P., Collins, W. D., Iacono, M. J., Easter, R. C., Ghan, S. J., Liu, X., Rasch, P. J., and Taylor, M. A.: Description of the NCAR Community Atmosphere Model (CAM 5.0), Tech. rep., National Center for Atmospheric Research, available at: http://www.cesm.ucar.edu/models/cesm1.0/cam/docs/description/ (last access: 11 November 2013), 2012. 9161

Nesbitt, S. W. and Zipser, E. J.: The diurnal cycle of rainfall and convective intensity according to three years of TRMM measurements, J. Climate, 16, 1456–1475, doi:10.1175/1520-0442-16.10.1456, 2003. 9158

Nordeng, T. E.: Extended versions of the convective parameterization scheme at ECMWF and their impact on the mean and transient activity of the model in the tropics, ECMWF Technical Memoranda 206, ECMWF, available at: http://www.ecmwf.int/publications (last access: 4 April 2014), 1994. 9188

Randall, D., Khairoutdinov, M., Arakawa, A., and Grabowski, W.: Breaking the cloud parameterization deadlock, B. Am. Meteorol. Soc., 84, 1547–1564, doi:10.1175/BAMS-84-11-1547, 2003. 9158

Stephens, G. L., L'Ecuyer, T., Forbes, R., Gettlemen, A., Golaz, J.-C., Bodas-Salcedo, A., Suzuki, K., Gabriel, P., and Haynes, J.: Dreary state of precipitation in global models, J. Geophys. Res., 115, D24211, doi:10.1029/2010JD014532, 2010. 9164

Stevens, B., Giorgetta, M., Esch, M., Mauritsen, T., Crueger, T., Rast, S., Salzmann, M., Schmidt, H., Bader, J., Block, K., Brokopf, R., Fast, I., Kinne, S., Kornblueh, L., Lohmann, U., Pincus, R., Reichler, T., and Roeckner, E.: Atmospheric component of the MPI-M Earth System Model: ECHAM6, J. Adv. Model. Earth Syst., 5, 146–172, doi:10.1002/jame.20015, 2013. 9161

ACPD
14, 9155–9201, 2014

Sundqvist, H., Berge, E., and Kristjánsson, J. E.: Condensation and cloud parameterization studies with a mesoscale numerical weather prediction model, Mon. Weather Rev., 117, 1641–1657, doi:10.1175/1520-0493(1989)117<1641:CACPSW>2.0.CO;2, 1989. 9188

Tiedtke, M.: A comprehensive mass flux scheme for cumulus parameterization in large-scale models, Mon. Weather Rev., 117, 1779–1800, doi:10.1175/1520-0493(1989)117<1779:ACMFSF>2.0.CO;2, 1989. 9188

Tiedtke, M.: Representation of clouds in large-scale models, Mon. Weather Rev., 121, 3040–3061, doi:10.1175/1520-0493(1993)121<3040:ROCILS>2.0.CO;2, 1993. 9188

Tobin, I., Bony, S., Holloway, C. E., Grandpeix, J.-Y., Sèze, G., Coppin, D., Woolnough, S. J., and Roca, R.: Does convective aggregation need to be represented in cumulus parameterizations?, J. Adv. Model. Earth Syst., 5, 692–703, doi:10.1002/jame.20047, 2013. 9182

Tost, H., Jöckel, P., and Lelieveld, J.: Influence of different convection parameterisations in a GCM, Atmos. Chem. Phys., 6, 5475–5493, doi:10.5194/acp-6-5475-2006, 2006. 9158, 9164

Waliser, D. E., Li, J.-L. F., Woods, C. P., Austin, R. T., Bacmeister, J., Chern, J., Genio, A. D., Jiang, J. H., Kuang, Z., Meng, H., Minnis, P., Platnick, S., Rossow, W. B., Stephens, G. L., Sun-Mack, S., Tao, W.-K., Tompkins, A. M., Vane, D. G., Walker, C., and Wu, D.: Cloud ice: a climate model challenge with signs and expectations of progress, J. Geophys. Res., 114, D00A21, doi:10.1029/2008JD010015, 2009. 9171

Zelinka, M. D. and Hartmann, D. L.: Response of humidity and clouds to tropical deep convection, J. Climate, 22, 2389–2404, doi:10.1175/2008JCLI2452.1, 2009. 9159

Zhang, G. J. and McFarlane, N. A.: Sensitivity of climate simulations to the parameterization of cumulus convection in the Canadian climate centre general circulation model, Atmos. Ocean, 33, 407–446, doi:10.1080/07055900.1995.9649539, 1995. 9188

ACPD
14, 9155–9201, 2014

Table 1. List of the observations used in this study along with their acronyms, horizontal resolutions, and the version of the dataset.

Variable	Source	Resolution	Version
Rain rate (RR) [mm h^{-1}]	TMPA	≈ 4 km	6/6A
Upper tropospheric humidity (UTH) [%RH$_i$]	AMSU-B	≈ 16 km	–
Cloud fraction (CF) [%]	2C-ICE	≈ 2 km	–
Cloud ice water content (IWC) [mg m^{-3}]	2C-ICE	≈ 2 km	–
Outgoing longwave radiation (OLR) [W m^2]	CERES	≈ 20 km	3A

ACPD
14, 9155–9201, 2014

Table 2. Some basic information about each model.

Model	Native grid	Levels	Top of model	Convection Scheme	Cloud scheme
CAM5	0.94° × 1.25°	30	10 hPa	Zhang and McFarlane (1995)	Gettelman et al. (2008) Morrison and Gettelman (2008)
EC-Earth 3	0.70° × 0.70°	91	0.1 hPa	Tiedtke (1989) Bechtold et al. (2004, 2008)	Tiedtke (1993); Forbes et al. (2011)
ECHAM6	0.90° × 0.90°	95	0.01 hPa	Tiedtke (1989); Nordeng (1994)	Sundqvist et al. (1989) Lohmann and Roeckner (1996)

ACPD
14, 9155–9201, 2014

Table 3. Area-weighted mean RR [mm h^{-1}] for the regions depicted in Fig. 1 plus those of the merged ocean and land regions.

Source	Atlantic	Indian	Pacific	Amazon	Africa	Ocean	Land
TMPA	0.12	0.17	0.13	0.16	0.09	0.14	0.12
EC-Earth	0.15	0.22	0.17	0.20	0.09	0.18	0.14
ECHAM6	0.14	0.23	0.19	0.20	0.10	0.18	0.15
CAM5	0.14	0.21	0.18	0.19	0.12	0.18	0.16

ACPD
14, 9155–9201, 2014

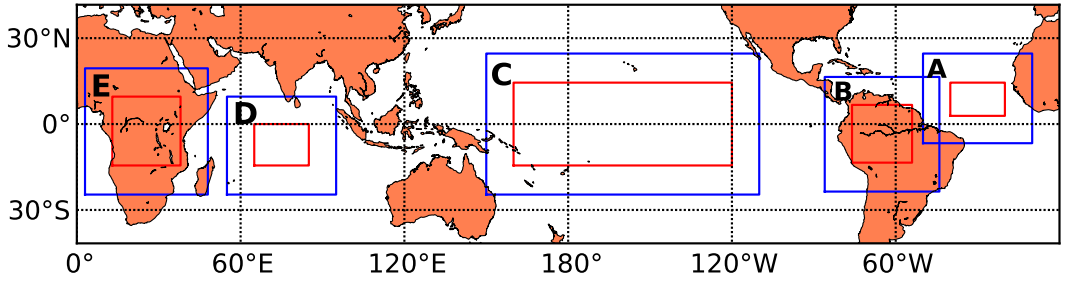

Fig. 1. Selected regions of deep convection across the Tropics: central Atlantic (A), the Amazon Basin (B), Pacific ocean (C), Indian ocean (D), and central Africa (E). Ocean-based regions are the combination of D, C and A and land-based regions are E and B. Red areas represent DC system centre regions, while blue boxes are data sampling regions.

ACPD
14, 9155–9201, 2014

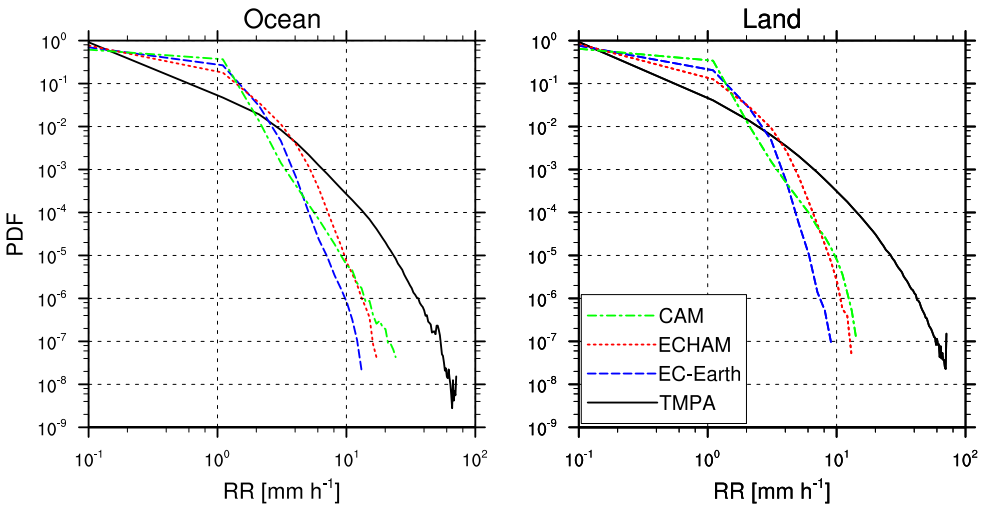

Fig. 2. Normalised PDF of surface rain rates for ocean-based (left plot) and land-based (right plot) for total precipitation of the merged regions described in Fig. 1.

ACPD
14, 9155–9201, 2014

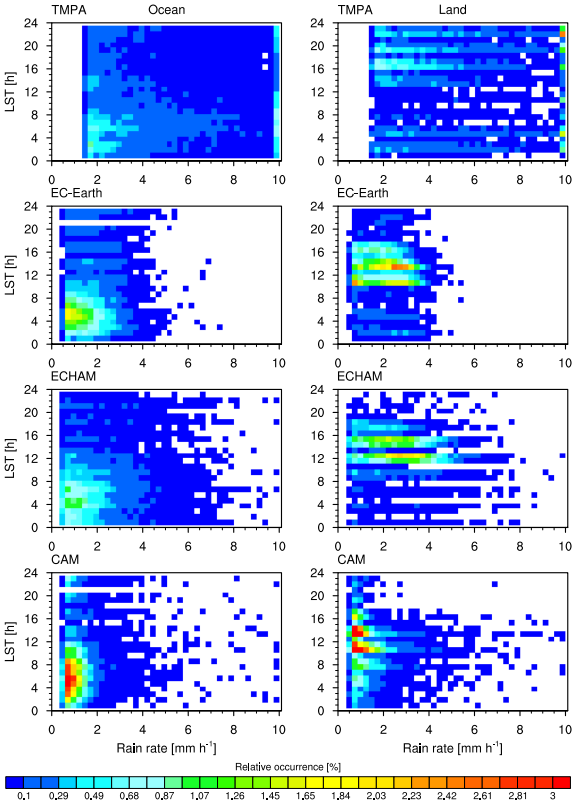

Fig. 3. Relative occurrence of selected DC systems as a function of RR and the LST of peak convection (i.e. the timing of "0 h" in the composite analysis). For each row, the results are given for TMPA, EC-Earth, ECHAM6, and CAM5 respectively. The RR bin size is set to 0.25 mm h^{-1} and one hour for the LST. The empty space for the lowest RR reflects the respective threshold values for the DC systems. The observations' RRs above 10.0 mm h^{-1} are mapped to 10.0 mm h^{-1} to reduce the spread of the data along the x axis.

ACPD
14, 9155–9201, 2014

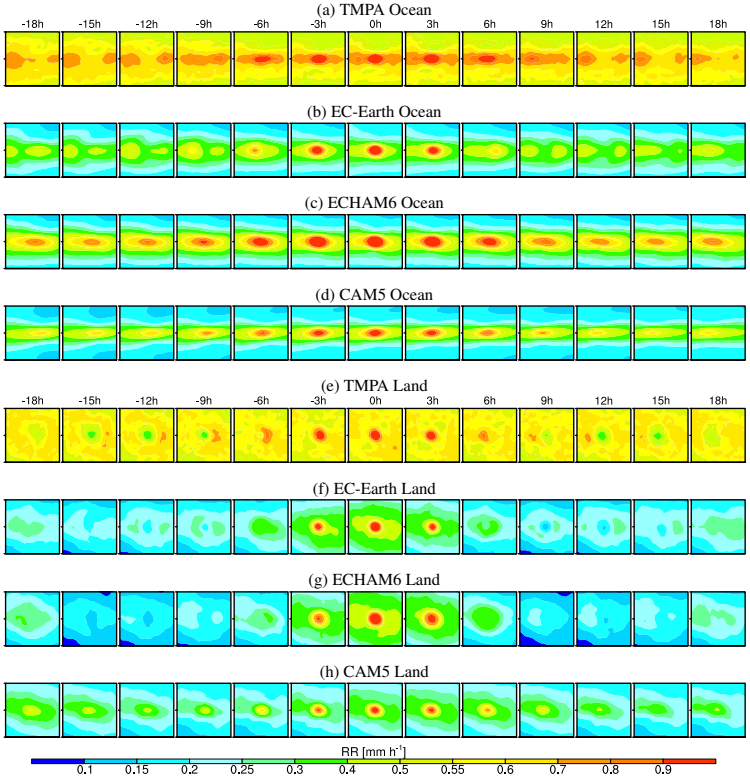

Fig. 4. Composite of RR for ocean-based **(a–d)** and land-based **(e–h)** systems for the observations followed by the models. The spatio-temporal coverage of ±18 h at every 3 h interval and ±10° longitude and latitude taken from the centre point and graduated every ±1°.

ACPD
14, 9155–9201, 2014

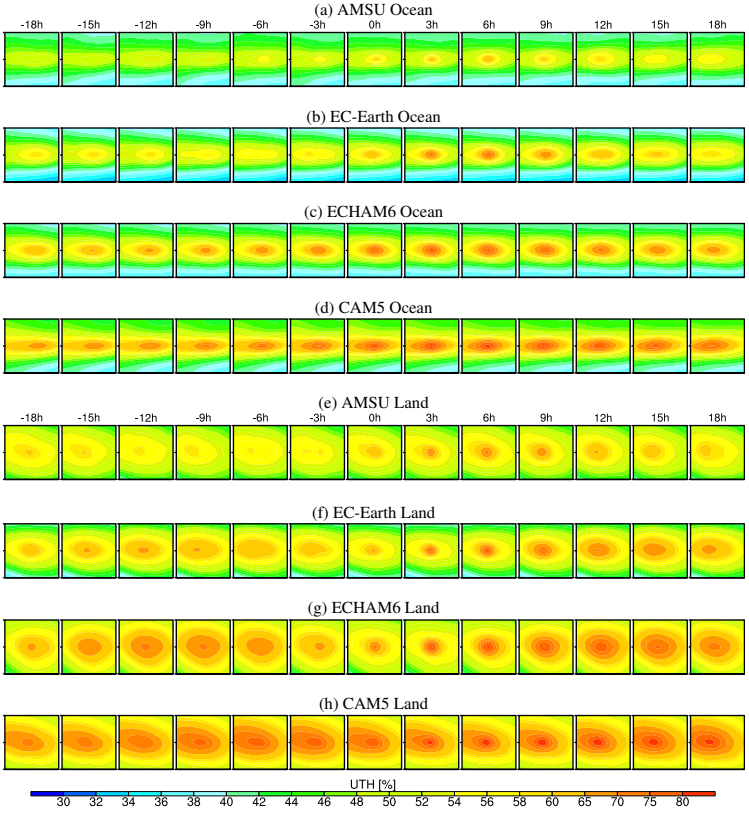

Fig. 5. As in Fig. 4, but for UTH.

ACPD
14, 9155–9201, 2014

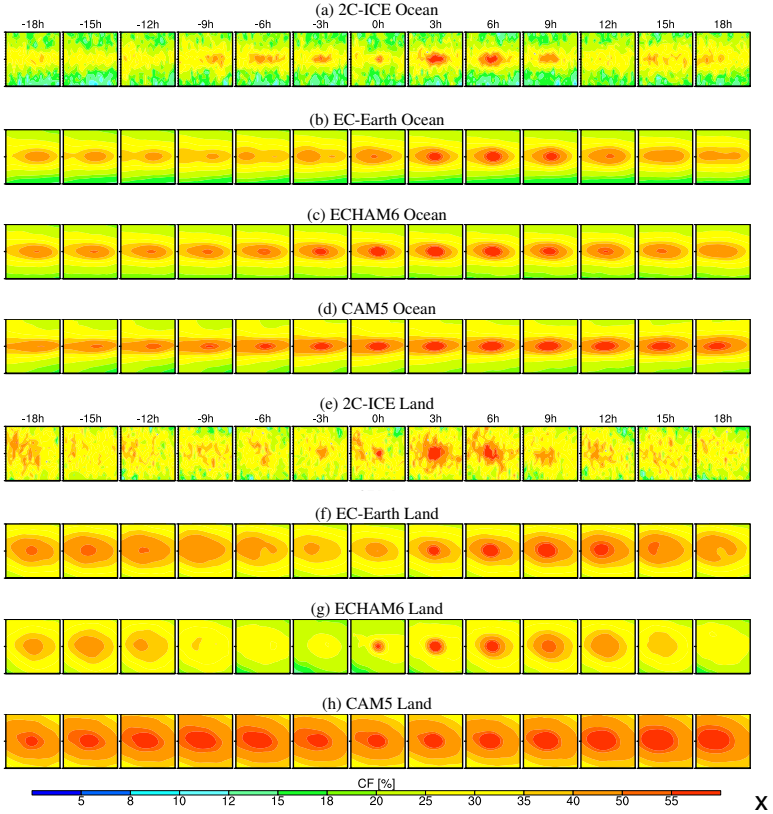

Fig. 6. As in Fig. 4 but for CF at 200 hPa.

ACPD
14, 9155–9201, 2014

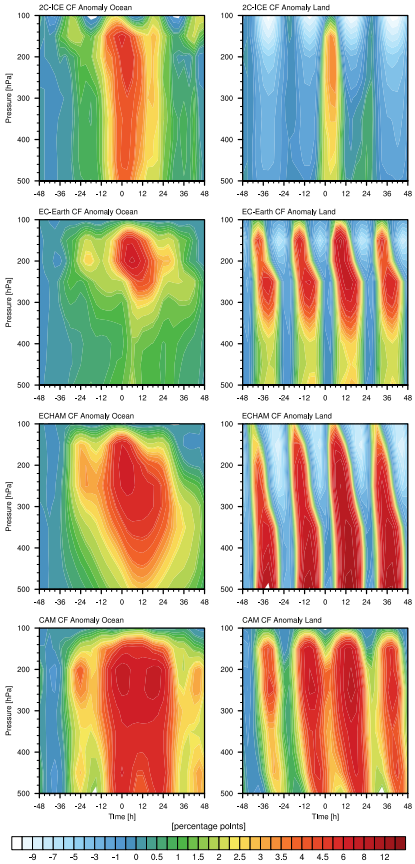

Fig. 7. CF anomaly for ocean-based (left column) and land-based (right column) systems. The data are plotted for the area ±3° latitude, ±10° longitude, and ±48 h from the centre point of peak RR. The observations are smoothed using a 12 h running mean. The background state is the spatio-temporal mean of the earliest 4 time bins.

ACPD
14, 9155–9201, 2014

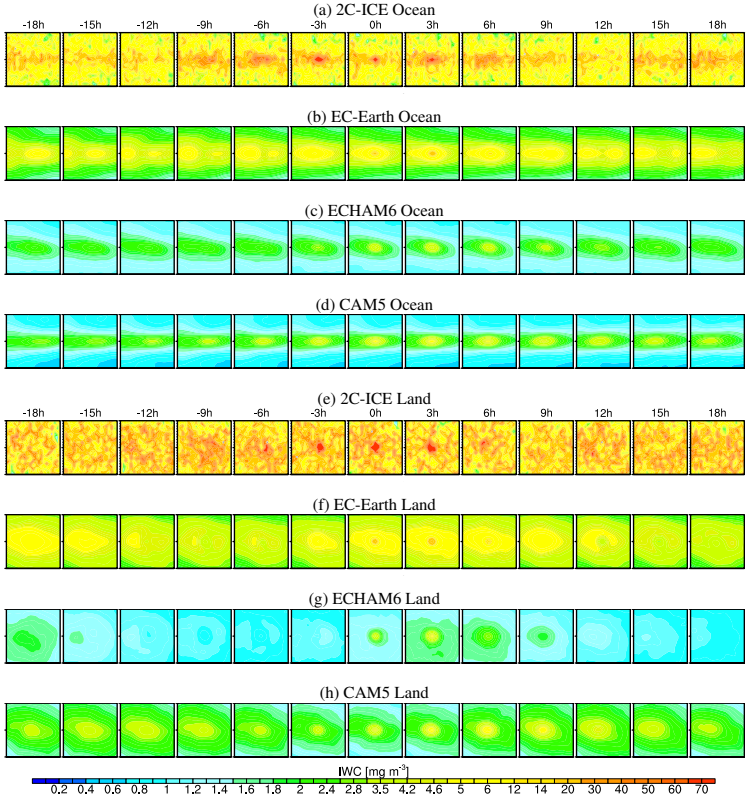

Fig. 8. As Fig. 4 but for IWC at 200 hPa.

ACPD
14, 9155–9201, 2014

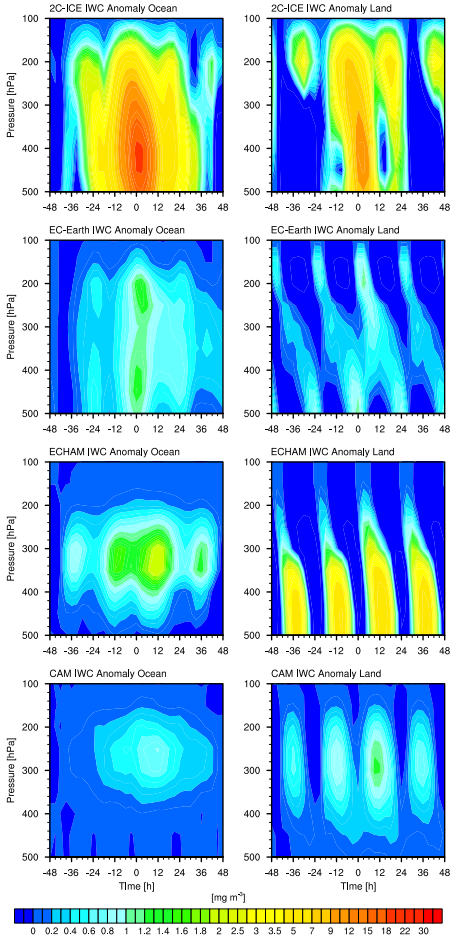

Fig. 9. As in Fig. 7 but for IWC.

ACPD
14, 9155–9201, 2014

Model intercomparison of deep convection in climate models

M. S. Johnston et al.

Fig. 10. As in Fig. 4 but for OLR.

ACPD
14, 9155–9201, 2014

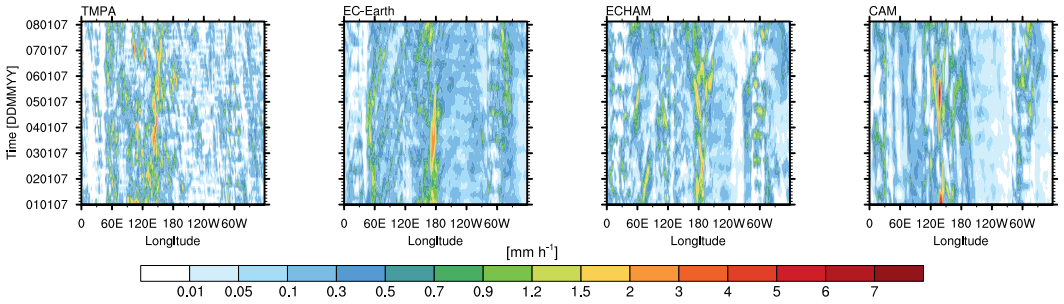

Fig. 11. Time-longitude illustration of all RRs across the tropics between ±5° latitude.

ACPD
14, 9155–9201, 2014

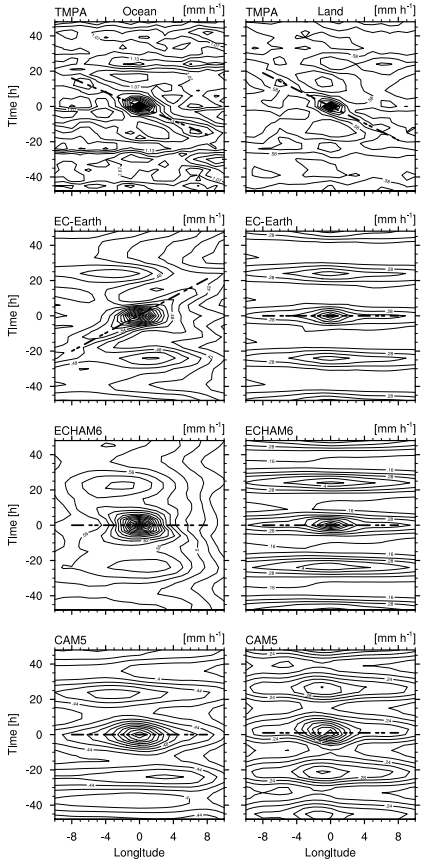

Fig. 12. Hovmöller diagrams of RRs centred on composite DC systems, for TMPA, ECHAM6, CAM5, and EC-Earth for (left) ocean-based systems and (right) land-based systems. The lines drawn on the figures are visual aids indicating the various directions of motion discussed in the text.

ACPD
14, 9155–9201, 2014